Florian Flatscher, BSc

The critical current density of garnet-based solid electrolytes

MASTER'S THESIS

to achieve the university degree of

Diplom-Ingenieur

Master's degree programme: Advanced Materials Science

submitted to

Graz University of Technology

Supervisor

Univ.-Prof. Dr.rer.nat. Martin Wilkening

Co-Supervisor

Mag.rer.nat. Dr.techn Daniel Rettenwander

Institute for Chemistry and Technology of Materials

Graz, June 2020

AFFIDAVIT

I declare that I have authored this thesis independently, that I have not used other than the declared sources/resources, and that I have explicitly indicated all material which has been quoted either literally or by content from the sources used. The text document uploaded to TUGRAZonline is identical to the present master's thesis.

Date, Signature

Acknowledgements

I would like to thank everybody at the Institute for Chemistry and Technology for Materials who supported me during my thesis.
I would especially like to thank my supervisor Daniel Rettenwander for the advice during the work and Prof. Wilkening for the possibility to do this project.
Further I would like to thank my family for their support and encouragement.

Contents

List of Figures

List of Tables

1 Introduction

Li-ion batteries with a liquid electrolyte used in some electric vehicles pose a significant safety issue due to the flammability of the liquid electrolyte[1]. Moreover, in crashes the fire fighting process is complicated due to the possibility to produce toxic compounds upon combustion, like hydrofluoric acid and organofluoric compounds[2]. The use of solid electrolytes poses an attractive alternative to liquid ones, since they solve the fire hazard, which could lead to all solid state batteries (ASSB). In 2011 Goodenough postulated a few requirements for solid electrolytes, which needed to be fulfilled in order to replace liquid electrolyte. They need to have a large electrochemical window, be chemically stable in ambient temperature and in temperatures occurring during battery use, be chemically stable against the electrodes, be able to cope with volume changes during charge and discharge, possess a high ionic conductivity, above 0.1 $mS{\cdot}cm^{-1}$, while also having a low electrical conductivity, below 0.1 $nS{\cdot}cm^{-1}$ while also being safe and cheap, just to name a few[3]. Unsurprisingly there are no materials, as of yet, that completely fulfill these demands. Regarding just the ionic conductivity, there are a few solid electrolytes that meet or exceed the necessitated conductivity. Those would be sulfide based materials with the composition of $Li_{4-x}Ge_{1-x}P_xS_4$ with an ionic conductivity of 2.2 $mS{\cdot}cm^{-1}$[4], $Li_{10}GeP_2S_{12}$ reaching around 12 $mS{\cdot}cm^{-1}$[5], or lithium-oxide garnets like $Li_7La_3Zr_{1.4}Ta_{0.6}O_{12}$ at 1 $mS{\cdot}cm^{-1}$[6].
$Li_7La_3Zr_2O_{12}$, short LLZO, is going the be the material of choice in this work. It normally crystallizes in a tetragonal structure with the space group $I4_1/acd$, possessing only a low ionic conductivity of 1.63 $\mu S{\cdot}cm^{-1}$[7]. It also possesses a high temperature cubic phase with the space group $Ia\bar{3}d$. The ionic conductivity of this phase is two orders of magnitude higher, at around 0.1 $mS{\cdot}cm^{-1}$[8]. Through the insertion of Al^{3+}, Ga^{3+} or Ta^{5+} into the crystal structure, the cubic phase can be stabilized at room temperature [9]. The electrochemical window of LLZO was first reported to be around 5.8 V[10]. This is only due to kinetic reasons, above 2.91 V LLZO decomposes to Li_2O_2, $Li_6Zr_2O_7$ and La_2O_3, which means it is only thermodynamically stable between 0.05 V and 2.91 V[11]. If the Ga^{3+} content is equal to or above 0.2 resulting in $Li_{6.4}Ga_{0.2}La_3Zr_2O_{12}$ the conductivity increases again to 1.2 $mS{\cdot}cm^{-1}$ due to the distortion of the crystal lattice and the transition to the space group $I\bar{4}3d$ creating additional lithium ion pathways [12]. It is relatively stable in atmosphere, though it forms a layer consisting of Li_2CO_3 and LiOH on its surface, with the CO_2 and the humidity in the air[13]. It is also rather stable against Li metal[14].
Historically Li metal batteries failed due to the same safety issues that still concern modern lithium ion batteries[15]. The flammability of the liquid electrolyte, which was further compounded by the growth of Li dendrites[16]. The usage of Li metal as an anode material would have the advantages of the highest possible theoretical capacity at

3862 mAh g^{-1} on the anode side, as well as the lowest possible electrode potential of -3.04 V, measured against the standard hydrogen electrode[17]. While LLZO is stable against Li, this is not the case for other classes of solid electrolytes. In Ti based solid electrolytes like $Li_{1+x}Al_xTi_{2-x}P_3O_{12}$ or $Li_{3x}La_{2/3-x}TiO_3$ the Ti_4^+ is reduced by the Li metal[18]. The afromentioned sulfide based materials decompose in contact with Li metal into its binary compounds, like Li_2S[19].

Next to the stability issues against Li, there also remains the problem of Li dendrites. Theoretical calculations in regard to polymer solid electrolytes showed that a high enough shear modulus of the material, about two times higher than the one of Li, might inhibit Li dendrite formation[20]. It was theorized that this could also be applicable for ceramic solid electrolytes. LLZO, which possesses a shear modulus of around 60 GPa, much higher than the shear modulus of Li with 5 GPa, was studied in this regard and dendrite formation was still observed[21][22][23]. It has also been monitored that dendrite formation occurs preferentially along grain boundaries in polycrystalline LLZO [24]. The exact mechanism behind dendrite formation and propagation is not yet understood. Different explanations for the mechanism behind dendrite formation in solid electrolytes have been proposed[25][26][27][28]. One of those is that existing defects cause preferential Li deposition during plating. Above a critical current density the over-potential during Li plating causes a high enough mechanical stress to fracture the solid electrolyte, creating a path along which the dendrite can grow[25]. Another explanation is that space charge layers form at the interface between the Li metal and the ceramic solid electrolyte through current induced pressure. The dendrite formation then occurs through an electrochemical mechanism, where it is more energetically favourable for the lithium to deposit in grain boundaries than at the interface, a "grain coating" process[26].

Dendrites are not the only problem that hinders all solid state batteries from becoming a reality. In contrast to a liquid electrolyte which, if given enough time, will contact the whole electrode surface, solid electrolytes have a more limited electrode contact area, leading to higher interfacial impedances[29]. The modification of the interface, such as through the application of interlayers, can be used to remedy this problem[30]. Reactions at the electrolyte-electrode interface can lead to the formation of a solid electrolyte interphase, SEI[31]. This also occurs in liquid electrolytes, where it is needed, since a passivation layer is formed and further reactions are stopped[16]. Both in liquid and in solid electrolytes this SEI needs to be self limiting and still have a ionic conductivity large enough to not inhibit the functionality of the battery[29]. For an all solid state battery the solid electrolyte also needs to be compatible with the cathode materials used. Problems that can occur here are lattice mismatch, space charge regions and the formation of inter diffusion layers. Due to their rigidity, oxide based solid electrolytes can not change their lattice to conform to the lattice of the cathode material. Volume changes in the cathode material during battery operation can then induce stress at the interface leading to an increase in interface impedance[32]. Sulfide based solid electrolytes should not be afflicted as much from lattice mismatch since they are softer[5]. Instead they suffer from the occurrence of a space charge layer when in contact with an oxide based high voltage cathode material like $LiMn_2O_4$ or $LiCoO_2$, which increases the interfacial impedance and

can be alleviated via a surface coating, stopping direct contact between the sulfide and the oxide[33][34]. Inter-diffusion between oxide based cathodes and solid electrolytes can also impede Li^+ ion diffusion and needs to be addressed with the introduction of buffer layers[32].
For the use in electric vehicles there is not only the need for high capacities, which could be in part provided by lithium metal as an anode, but there is also the need for fast charging, necessitating applicable current densities of at least 3 $mA \cdot cm^2$ [35]. The critical current density, short CCD, at which lithium dendrites begin to form is in the $\mu A \cdot cm^2$ range for LLZO[36][22][24]. The exact cause for the low CCD is not yet known and there are a variety of possible influences like grain size[37], dopants[38] or the Li|LLZO interface[27].
In this work the connection between the Li|LLZO interface and the CCD is the main focus. For this purpose single crystals of $Li_{6.4}Ga_{0.2}La_3Zr_2O_{12}$ are used in order to eliminate grain boundaries, density, compositional differences and other sample inconsistencies as causes for the CCD. Different methods are employed to prepare a good interface and to reduce the area specific resistance, ASR, of the Li|LLZO interface to a varying degree. These include several polishing steps in air, as well as further polishing in an Ar filled glovebox followed by a 400 °C heat treatment inside the glovebox in order to create a flat LLZO surface, which is as devoid of contaminating layers as possible[13]. To further reduce the ASR, heat treatments of the lithium LLZO interface are employed [22]. The application of thin Au interlayers between the LLZO and the lithium, which forms an alloy with Li upon heating, is also utilized to improve the ASR[27][39]. Through galvanostatic cycling until occurrence of a short circuit, the critical current density is determined as a function of the ASR, which was measured via impedance spectroscopy.

2 Theory

2.1 Impedance Spectroscopy

In impedance spectroscopy a sinusoidal AC signal with varying frequency is applied to the sample and the current response is measured, which can have a shifted phase in regard to the input signal. With the current, voltage and phase shift, material properties like impedance, conductance and permittivity can be calculated. The relationship of current and voltage with the frequency is shown in equations 2.1 and 2.2.

$$V(t) = V_m \cdot sin(\omega t) \tag{2.1}$$

$$I(t) = I_m \cdot sin(\omega t - \theta) \tag{2.2}$$

Here V_m is the maximum applied voltage, I_m the maximum applied current, θ the phase shift and ω the angular frequency. This expression can be rewritten in an exponential form, as shown in the equations 2.3 and 2.4.

$$V(t) = V_m \cdot exp(j\omega t) \tag{2.3}$$

$$I(t) = I_m \cdot exp(j(\omega t - \theta)) \tag{2.4}$$

$$j = \sqrt{-1} \tag{2.5}$$

The impedance is defined according to equation 2.6, which leads to equation 2.7 after inserting equations 2.3 and 2.4.

$$Z(\omega) = \frac{V(t)}{I(t)} \tag{2.6}$$

$$Z(\omega) = \frac{V_m}{I_m} \cdot exp(j\theta) \tag{2.7}$$

The exponential function can then be rewritten as a sum of a real and an imaginary wave function according to Euler's law, shown in equation 2.8 and the absolute value of

the impedance is shown in the equation 2.9. With this the real and the imaginary part of the impedance can be defined, as shown in the equations 2.10 and 2.11.

$$Z(\omega) = \frac{V_m}{I_m} \cdot (cos(\theta) + j \cdot sin(\theta)) \tag{2.8}$$

$$|Z(\omega)| = \frac{V_m}{I_m} \tag{2.9}$$

$$Z'(\omega) = |Z(\omega)| \cdot cos(\theta) \tag{2.10}$$

$$Z''(\omega) = |Z(\omega)| \cdot j \cdot sin(\theta) \tag{2.11}$$

In an ideal resistor the current and voltage behave according to Ohms law, shown in equation 2.12. With the voltage given by equation 2.1 the current can be determined and both can be inserted into equation 2.6. This leads to the impedance of an ideal resistor shown in equation 2.13, with no phase shift occurring.

$$V(t) = R \cdot I(t) \tag{2.12}$$

$$Z(\omega) = R \tag{2.13}$$

In an ideal capacitor the capacitance C is defined according to equation 2.14, where Q is the electric charge. With the help of equation 2.1 this can be rewritten to equation 2.15. Current is defined as the change in electric charge over time, as written in equation 2.16, which then leads to the current voltage behaviour in a capacitor shown in equation 2.17. Rearranged and inserted into equation 2.8 this leads to the impedance of an ideal capacitor, denoted in equation 2.18. With the input voltage following a sin wave as stated in 2.1 and the current in a capacitor following a cosin wave according to equation 2.17 there is a phase shift of the current of $\frac{\pi}{2}$ ahead of the voltage.

$$Q = C \cdot V \tag{2.14}$$

$$Q = C \cdot V_m \cdot sin(\omega t) \tag{2.15}$$

$$I(t) = \frac{dQ}{dt} \tag{2.16}$$

$$I(t) = C \cdot V_m \cdot \omega \cdot cos(\omega t) \tag{2.17}$$

$$Z(\omega) = \frac{1}{j\omega C} \tag{2.18}$$

The relation of inductance, written as L with the unit Henry, to voltage and current is shown in equation 2.19. Inserting equation 2.1, rearranging and integrating it, leads to equation 2.20, which can again be inserted into equation 2.8 to deliver the impedance of an ideal inductor shown in equation 2.21. Similar to the capacitor current is phase shifted $\frac{\pi}{2}$ behind the voltage.6

$$V(t) = L \cdot \frac{dI(t)}{dt} \tag{2.19}$$

$$I(t) = \frac{V_m}{\omega L} \cdot sin(\omega t - \frac{\pi}{2}) \tag{2.20}$$

$$Z(\omega) = j\omega L \tag{2.21}$$

There are a few ways to display the results of an impedance spectroscopy measurement. The most common ones are the Bode plot, where the real part of the conductivity σ is plotted against the frequency ω and the Nyquist plot, where the negative imaginary part of the impedance (-Z") is plotted against the real part of the impedance (Z'). For the purpose of this work the main focus is going to be on the Nyquist plot.

With the equations for the impedance of an ideal resistor 2.13, an ideal capacitor 2.18 and an ideal inductor 2.21 and the knowledge of their respective phase shifts, their influence on the position of a measurement point in a Nyquist plot can be determined. An ideal resistor has no phase shift, so a measured point can only be on the real part of the plot, on the x axis, depending on its resistance. An example Nyquist plot for an ideal resistor is shown in Figure 2.1.

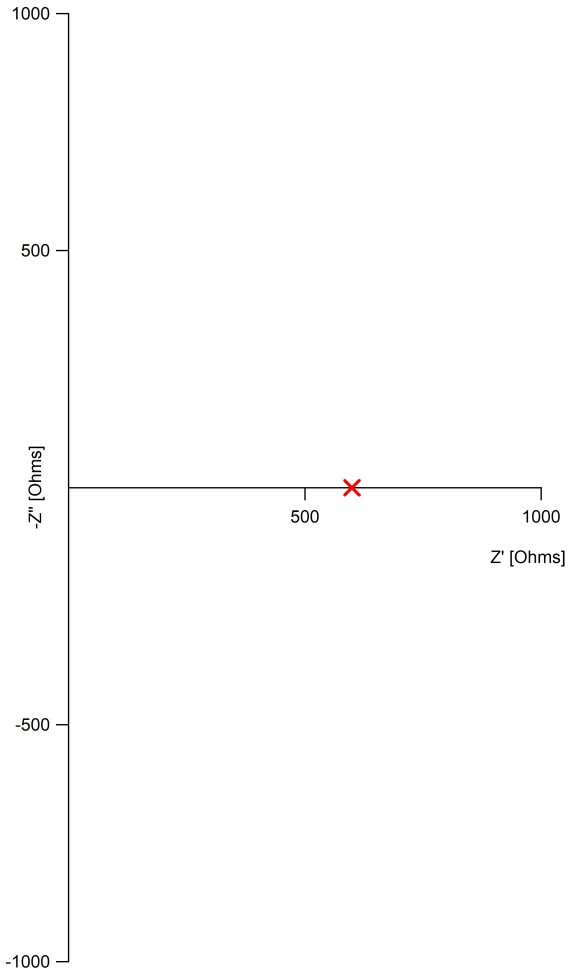

Figure 2.1: Nyquist plot of an ideal Resistor

An ideal capacitor on the other hand is phase shifted by $+\frac{\pi}{2}$, which means it is only going to influence the position on the imaginary part of the plot, on the y-axis. Since the negative imaginary part of the impedance is plotted, the measured point will be shifted up the y-axis according to the capacitance. The corresponding Nyquist plot for an ideal capacitor is shown in Figure 2.2.

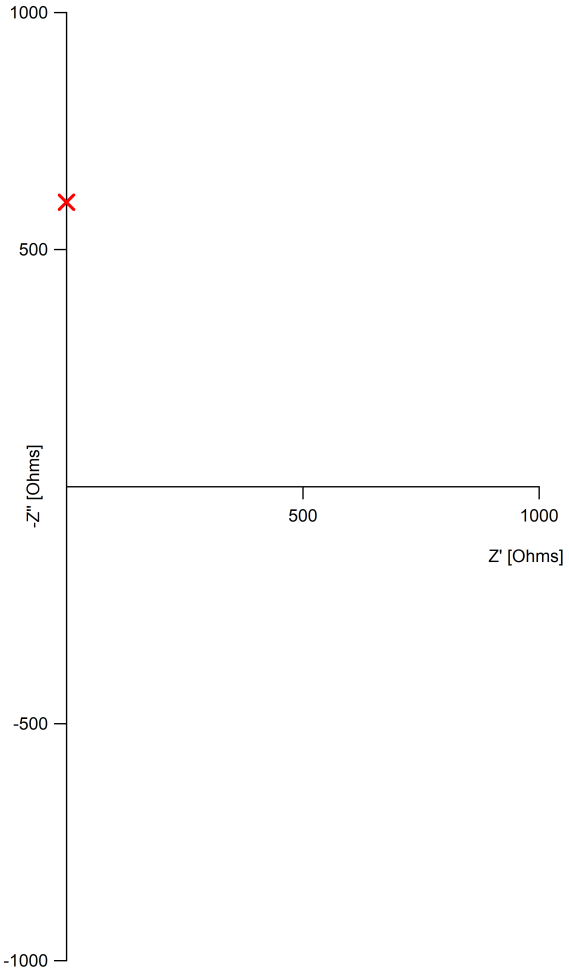

Figure 2.2: Nyquist plot of an ideal Capacitor

For an ideal inductor there is a similar behaviour, only phase shifted by - $\frac{\pi}{2}$. This means that the measured point will be shifted down the y-axis according to the inductance. An example Nyquist plot for an ideal inductor is shown in Figure 2.3.

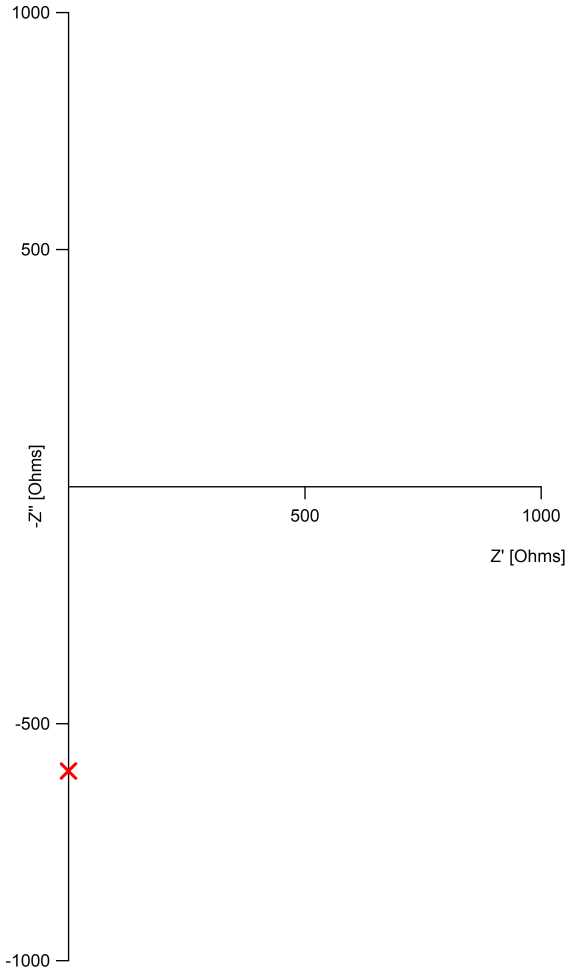

Figure 2.3: Nyquist plot of an ideal Inductor

While these ideal circuit elements give a helpful indication for the cause of the signal, individually they are not enough to accurately describe the behaviour of a real material. In order to accomplish this, an equivalent circuit is created with those elements connected in parallel or in series. For a ceramic solid state electrolyte the typical equivalent circuit is a resistor and a capacitor in parallel and there is almost no inductive behaviour expected. The Nyquist plot for such an equivalent circuit is shown in Figure 2.4.

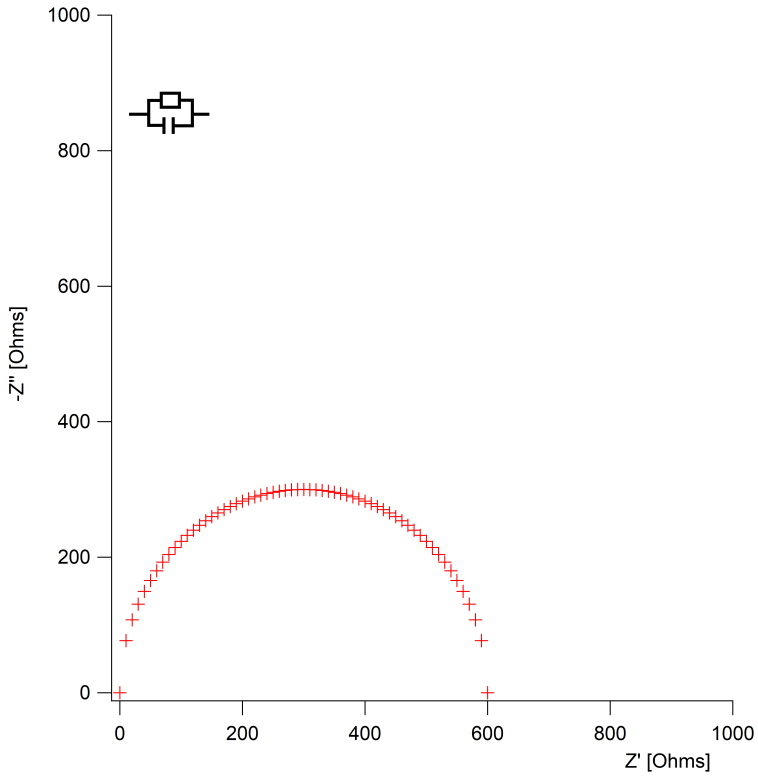

Figure 2.4: Nyquist plot for an parallel circuit of a resistor and a capacitor

If there was no correlation between the electric current and the ion motion in the material, such an ideal semicircle, with its center intersecting with the x-axis, can be expected. On the other hand if the center of the semicircle is below the x-axis there is a correlation between ion motion and the application of an electric current. This leads to a behaviour that does not correspond any more to an ideal capacitor in parallel with a resistor[40]. For a solid electrolyte, which does not solely depend on its native ion diffusion to work, this is to be expected. In the equivalent circuit this is taken into account by swapping the capacitor with a constant phase element (CPE), which takes the non ideal capacitive behaviour into account. The impedance for just a CPE element is written in equation 2.22. The Nyquist plot for a resistor in parallel with a CPE element, a R-CPE circuit, is shown in figure 2.5

$$Z(\omega) = \frac{1}{(j\omega)^{\alpha} Q} \tag{2.22}$$

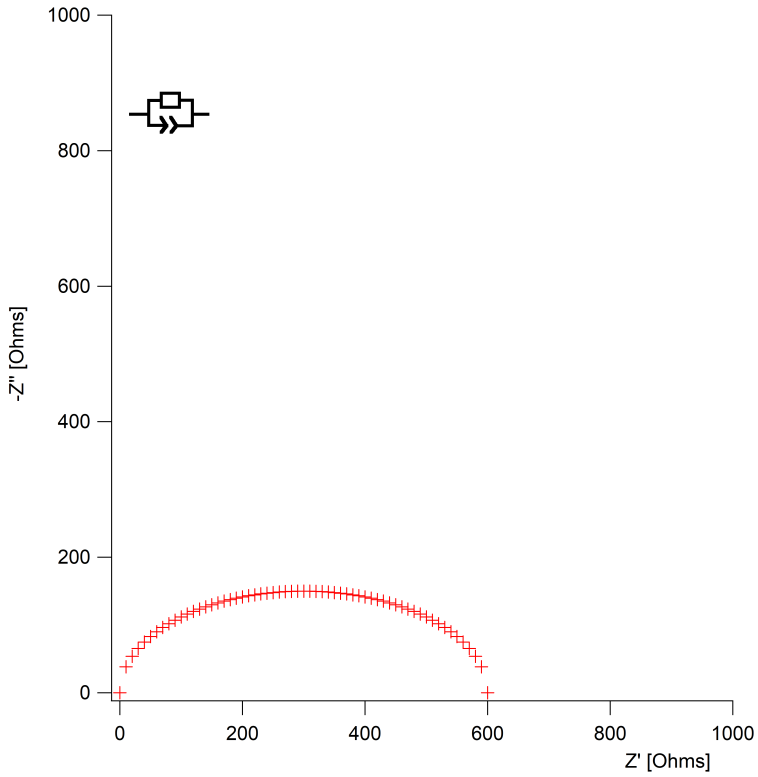

Figure 2.5: Nyquist plot for a parallel circuit of a resistor and a CPE

A parallel R-CPE circuit describes a single crystal electrolyte well, disregarding interfacial interactions and low frequency diffusion based impedance responses. For polycrystalline electrolytes an additional R-CPE circuit in series is needed to take into account a semicircles caused by grain boundary interactions. A further R-CPE circuit is needed if there are reactions at the electrolyte electrode interface or surface reactions. The semicircles and their causes can be distinguished by their capacitance and in turn their relaxation time. The relationship of relaxation time τ and capacitance is shown in equation 2.23.

$$\tau = R \cdot C \tag{2.23}$$

Bulk processes have the fastest relaxation time with a capacitance in the pF range. Grain boundary interactions are slower with a capacitance in the nF range. Interface and Surface reactions occur at even lower frequencies with a capacitance in the µF range for interface and a capacitance at around 10 µF for surface reactions. Further interactions and their respective capacitances are mentioned in a paper of Irvine[41].
For a single crystalline material with lithium electrodes on both sides, two semicircles are expected, one for the bulk process and one for the interface reaction. To ensure

the comparability of the interface impedance Z_{Int} it is normalized to the area specific resistance, ASR, with the unit $\Omega \cdot cm^2$. The exact relation is shown in equation 2.24.

$$ASR = \frac{Z_{Int} \cdot A}{2} \tag{2.24}$$

2.2 GCPL

Galvanostatic cycling with potential limitation (GCPL) is a common technique used to elucidate battery characteristics. A constant current is sent through the sample and the voltage is measured. With this the capacity, reversibility and the stability of the sample over multiple cycles can be determined. The potential limit can be used to stop the charging and discharging process at a certain point. For instance if only the repeated charge and discharge from 80 % to 100 % and vice versa is to be observed. Further explanation in regard to the use of this technique can be found in the reference[42].

3 Experimental

3.1 Initial sample preparation outside

The received $Li_{6.4}Ga_{0.2}La_3Zr_2O_{12}$ single crystals were first dry polished in air at a Struers LapoPol 25 at around 200-300 RPM with SiC grinding paper ranging from grit size of 220 to 4000 to create parallel sides and to remove Li_2CO_3 and LiOH layers on the surface of the LLZO. Upon completion of the polishing the samples were first scratched with a glass cutter and then broken into smaller pieces to increase the number of samples. They were then transferred into an Ar filled glovebox as soon as possible, to hinder the Li_2CO_3 and LiOH layers from reforming.

3.2 Sample preparation in the Glovebox

In the glovebox they were then put into an Alumina crucible, placed into an oven and heated to 400 °C for 3 h to remove contaminating layers that may have formed on the surface, mainly LiOH according to Ref.[13]. After the heat treatment a rainbow-like sheen remained on the crystals.

Figure 3.1: A rainbow-like sheen is visible on the bottom half of the LLZO single crystal. Better capture of the sheen was hindered due to reflection in the glovebox window.

Then the single crystals were polished manually with SiC grinding paper ranging from grit size 500 to 4000 to remove the rainbowlike sheen, which might have been a Li_2CO_3 layer that formed after the heating or during storage. One sample was tested without polishing to confirm this hypothesis. The results are explained in detail in section 4.1.1 After a last polish with SiC grinding paper grit size 4000 before any measurement, the passivated layer of a piece of Li foil was scraped away with a scalpel and two pieces with a diameter of 2,5 mm were punched out. They were placed on both sides of the crystal and covered with a copper current collector each, to facilitate easier removal of the sample after the heating step.

3.3 Impedance measurement and heat treatment

The sample was then placed into a custom-made heat resistant Swagelok-like cell. Through the cell a slight pressure is applied to the sample. The cell was connected to a Novocontrol Alpha/Beta Analyzer and the impedance was measured from a range of 10 MHz to 0.1 Hz with an amplitude of 5-10 mV. Then the sample was transferred to a vacuum line and heated to improve the contact between the Li and the LLZO.

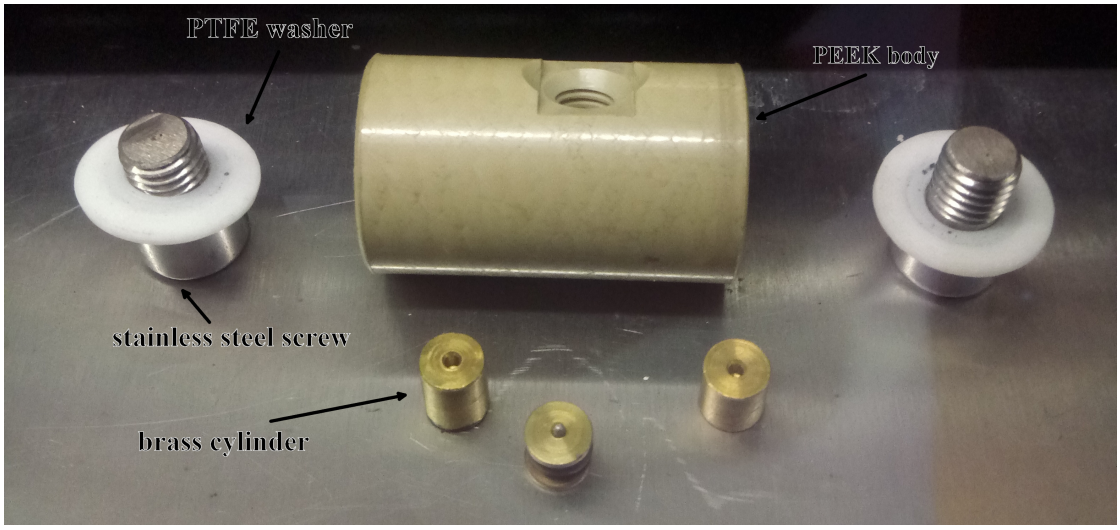

Figure 3.2: Disassembled custom Swagelok-like cell, consisting of the PEEK main body, two brass cylinders, a brass part with a rubber insert to replace a normal spring and two stainless steel screws with PTFE washers to seal the cell. Not visible is the third stainless steel screw with a PTFE washer to seal the side opening.

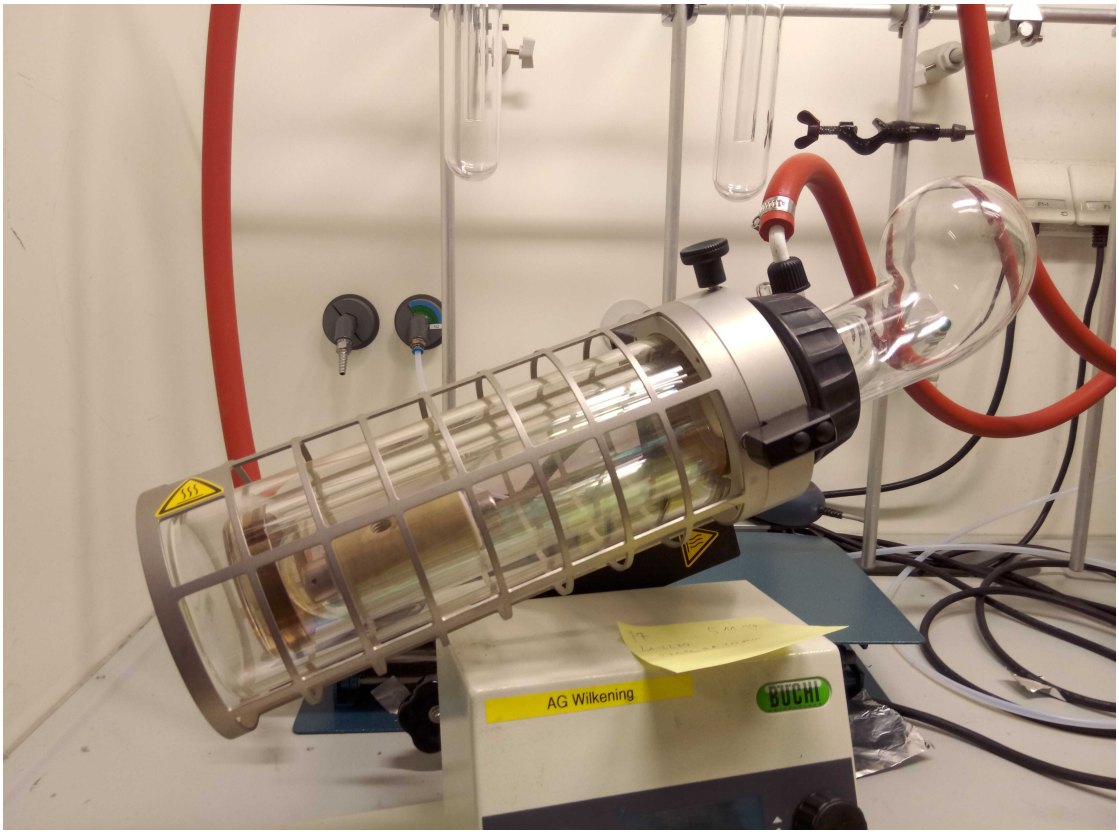

Figure 3.3: The custom made Swagelok-like cell placed in the vacuum line for heating. The open side allows gases that may form during the heating to escape.

Different heating temperatures (120 °C - 175 °C) and hold times (1 h - 7 h) were tested in regard to their efficacy to improve the contact. The vacuum line was used to rule out any reaction with contaminants that might be contained in the glovebox, like CO_2 or N_2 and to reduce reactions with gases that escape from the rubber tube used as substitute for metal springs, since metal springs can interfere with impedance measurements. After the sample cooled down to room temperature, it was transferred back into the glove box and the impedance measurement was repeated.

3.3.1 Application of a gold interlayer

For a few samples an improvement of the interface by depositing a 5 nm layer of gold on top of the LLZO according to Ref.[27] was tested. The polished samples were covered with an insulating tape, which had a 2,5 mm hole punched out and were placed in the sputtering chamber. A 5 nm layer of gold was sputtered onto the sample through the hole in the tape. The tape was used to avoid a continuous gold layer on the edges of the sample, which could lead to a short circuit while contacting the sample. Li was placed on the samples as described above, the impedance of the samples was measured, then

the samples were heated. One sample was heated in a vacuum line at 175 °C for 6 h, as described above. Two samples were heated in the glovebox on a resistive furnace to 175 °C for around two minutes on both sides. The temperature was measured via a thermocouple in contact with the single crystal and the process was observed via an optical microscope. After the samples were cooled to room temperature the impedance was measured again.

3.4 Cycling of the Samples

If the ASR was at an acceptable level the cell was cycled with a constant current and a half cycle duration of 20 minutes [22]. First trials were done with a Biologic SMP 50 in the glovebox and, with the samples transferred to a normal Swagelok cell and a second impedance measurement before cycling, with a Biologic VMP3 and MPG2 outside of the glovebox. The resolution available with the Biologic devices, which are not designed for accurate low current measurements, was rather low. Furthermore, after disassembly of the cells in the glovebox, the lithium on the LLZO showed signs that it reacted with the atmosphere. Therefore, later measurements were done in the glovebox with a Keithley 2450 SMU and a custom made LabView program. The starting current density was 1 $\mu A \cdot cm^{-2}$, after each cycle it was increased first to 5 $\mu A \cdot cm^{-2}$, then 10 $\mu A \cdot cm^{-2}$ and 20 $\mu A \cdot cm^{-2}$ after which the current density increased in 20 $\mu A \cdot cm^{-2}$ steps until a short circuit occurred.

4 Results and Discussion

4.1 Improvement of the Interface Resistance

4.1.1 The necessity of polishing

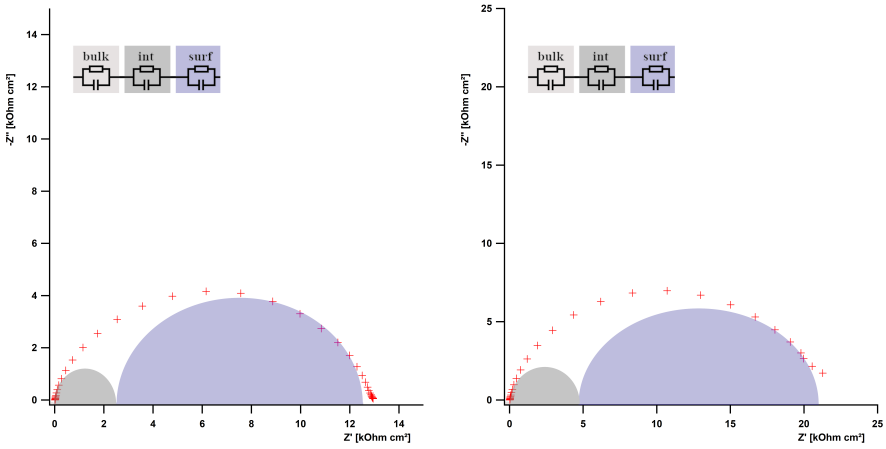

Figure 4.1: On the left the impedance of the non-polished sample is shown before heating, on the right after heating to 175 °C for 7 h. The equivalent circuits used to fit the data are depicted on the top left. The resonance frequency of the interface process is denoted. Semicircles have been added to approximately represent the individual contributions.

In the figure 4.1 the Nyquist plots before and after heating can be seen for the sample that was not polished after heating the single crystal to 400 °C in the oven. The ASR is in the $k\Omega \cdot cm^2$ range before heating and after heating to 175 °C for 7 h. The heating seemingly does not lower the ASR. The exact determination of the ASR is difficult in this case, since the plot can not be fitted with just an equivalent circuit for a bulk and an interface process. The second semicircle dominates the Nyquist plot here, to such an extend that the bulk semicircle is not even visible. There seems to be a second contribution next to the interface process to this semicircle. A separation of these two was not possible. The most likely cause is a remaining Li_2CO_3 contamination layer on the LLZO single crystal, which has a poorer wettability in regard to Li metal than LLZO reducing the effective contact area[13].

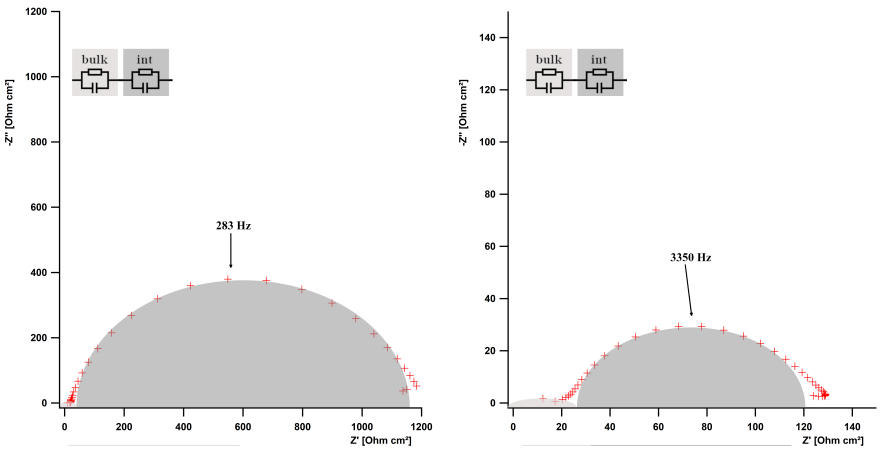

Figure 4.2: On the left the impedance of the polished sample is shown before heating, on the right again after heating to 175 °C for 7 h. The equivalent circuits used to fit the data are depicted on the top left. The resonance frequency of the interface process is denoted. Semicircles have been added to approximately represent the individual contributions.

The figure 4.2 shows the Nyquist plots before and after heating of the same sample, after it was polished in the glovebox and lithium was applied again. The ASR before heating is lower than for the unpolished sample at around 1.1 k$\Omega \cdot cm^2$. After heating the sample the Li-LLZO contact improves and the ASR reduces to around 100 $\Omega \cdot cm^2$. This time there was no other contribution to the second semicircle other than the interface process. Therefore it seems likely that the cause was indeed a contamination layer, which can be successfully removed via polishing in inert atmosphere.

4.1.2 ASR improvement via Au interlayer

The usage of thin metal layers on LLZO to improve the ASR is already well known in literature and a variety of materials have been already been used like Al[43], ZnO[44] and Au[27]. The basic premise is that the thin metal layer has a better reactivity with Li metal than LLZO itself, allowing the lithium to contact the whole metal layer. Upon heating an alloy is formed with the metal bringing the lithium in contact with the LLZO again. Here 5 nm gold layers were used to improve the ASR. The figure below shows the Nyquist plot of the Li|Au|LLZO|Au|Li sample before and after heating to 175 °C for 6 h.

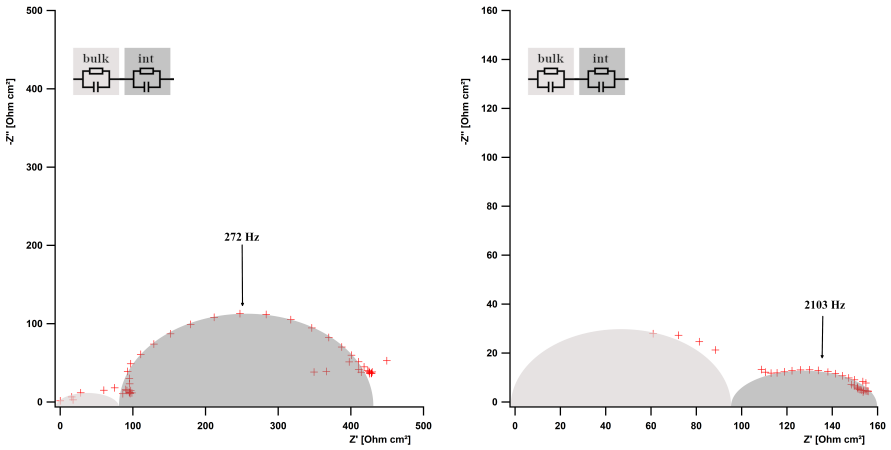

Figure 4.3: On the left the impedance normalized in regard to the area before heating can be seen. On the right the normalized impedance in regard to the area can be seen after 6 h at 175 °C in a vacuum line. The equivalent circuits used to fit the data are depicted on the top left. The resonance frequency of the interface process is denoted. Semicircles have been added to approximately represent the individual contributions.

On the left the Nyquist plot can be seen directly after the lithium has been applied, with the ASR being at around 300 $\Omega \cdot cm^2$. On the right there is the Nyquist plot after heating to 175 °C for 6 h in the vacuum line and the ASR has been reduced to 30 $\Omega \cdot cm^2$. The bulk part of the Nyquist plots stays the same and is not changed due to the heating process. In the Nyquist plot after heating, it is merely magnified as a result of the lowered ASR. Through the application of a gold layer a clear improvement of the ASR for the interface can be seen. This is due to the formation of a Li-Au alloy at around 170 °C, which leads to better wetting.
For the samples, which were heated in the glovebox the heating time was varied, to see if it was possible to achieve different ASR values for the interface. During the heating the formation of the Li-Au alloy could clearly be seen, when the black color of the 5 nm Au layer changed to white at 170 °C. The figure 4.4 shows the gold layer and the lithium during the heating.

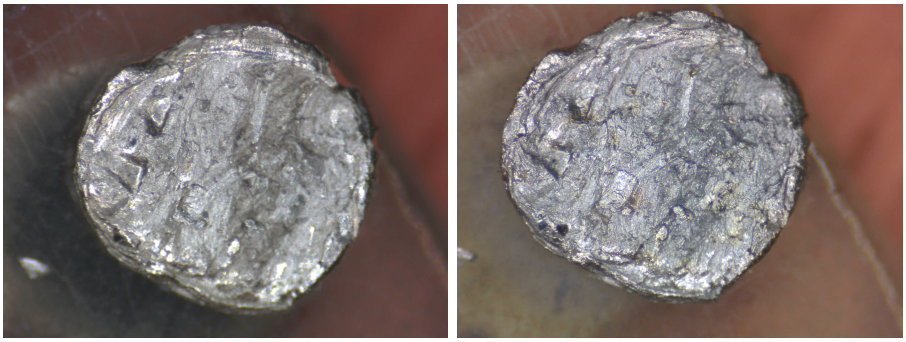

Figure 4.4: On the left the sample is at 160 °C. The gold layer still has its black color and the lithium is seen slightly off center on the gold layer. On the right the temperature is at 170 °C and the alloy has formed, the gold layer is now white.

The corresponding Nyquist plots before and after, depicted below in figure 4.5, show that heating the sample to 175 °C for just a few minutes is enough to drastically lower the interface ASR from the $k\Omega \cdot cm^2$ range to just 160 $\Omega \cdot cm^2$. The extended semicircle in the plot on the left could be due to an overlap of the interface semicircle with a semicircle belonging to a surface reaction, since the Li is not only on the gold layer. An exact separation during fitting was not possible, since multiple combinations could be used to get the same result.

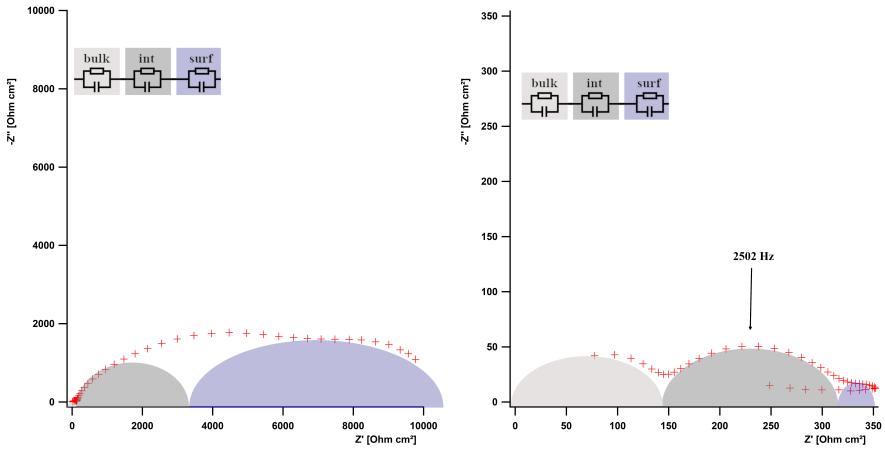

Figure 4.5: On the left the impedance normalized in regard to the area before heating can be seen. On the right the normalized impedance in regard to the area can be seen after a few minutes at 175 °C on a ceramic oven. The equivalent circuits used to fit the data are depicted on the top left. The resonance frequency of the interface process is denoted. Semicircles have been added to approximately represent the individual contributions.

The high initial interface ASR is most likely due to inaccurate placement of the lithium on top of the gold layer, as can be seen in figure 4.4. Therefore this experiment was repeated with a larger area for the gold layer to facilitate easier lithium placement. This is shown in figure 4.6.

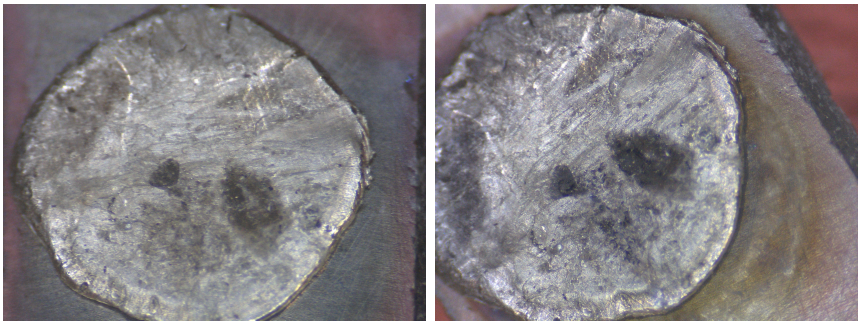

Figure 4.6: On the left the sample is shown before heating. On the right the sample is shown at 170 °C. The alloy formation can be seen in the changing color of the gold layer.

The Nyquist plots in figure 4.7 show a similar result as the experiment before, the interface ASR reduces from 500 $\Omega \cdot cm^2$ to 30 $\Omega \cdot cm^2$. There is also a third semicircle visible in the heated sample, which might be due to a surface reaction between LLZO and lithium. This time the initial ASR is much lower, most likely due to the lithium only being in contact with the gold and not with the LLZO itself.

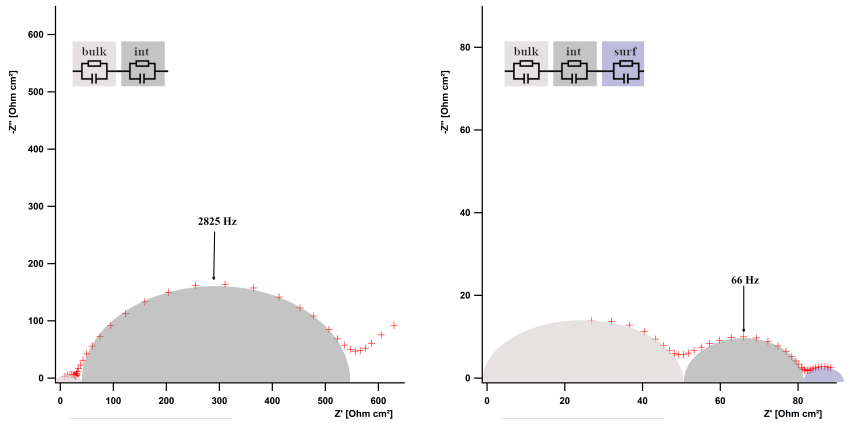

Figure 4.7: On the left the impedance normalized in regard to the area before heating can be seen. On the right the normalized impedance in regard to the area can be seen after a few minutes at 175 °C on a ceramic oven. The equivalent circuits used to fit the data are depicted on the top left. The resonance frequency of the interface process is denoted. Semicircles have been added to approximately represent the individual contributions.

This shows that the use of a gold interlayer indeed reduces the ASR of the interface. Unfortunately this also makes this method non-viable for a systematic study of the critical current density in regard to the ASR. Fine tuning the interface ASR with a gold interlayer is not possible through a variation of the heating time. Using a mix of samples with gold interlayers for low ASR values and samples without interlayers for higher ASR values would make the comparison harder by introducing an additional element able to cause a change in the CCD. Therefore the use of gold interlayers to improve the ASR was dropped.

4.1.3 ASR improvement via heating

The idea behind the heating is, that although lithium is a rather soft metal and can be pressed onto the surface of the single crystal with ease, it will not conform perfectly to the surface, leaving voids in between. This means that the area of the lithium piece, with a diameter of 2,5 mm, does not correspond to the surface area, that is in contact with the single crystal. Heating the lithium close to its melting point, which is at 180,5 °C, softens it further and through the slight pressure applied by the Swagelok-like cell, it should conform better to the surface. The success of this treatment can be seen in 4.1, where the ASR before and after heating is shown for different hold times and temperatures. It has to be noted that the heating could also increase the area of the lithium itself, which can also reduce the ASR, since it is normalized in regard to the area. Checking this is rather difficult, since removing the copper foil from the lithium after heating, to determine the area accurately, tends to rip the lithium with it off the single crystal. Therefore the calculations regarding the ASR were done with the initial area of the lithium piece, with a diameter of 2,5 mm. While the heating tends to reduce the ASR, there is no clear correlation visible between the heating time and the relative reduction in the ASR, since heating it to 175 °C for 7 hours produced better as well as worse results than heating it to 175 °C for only 1 hour. The initial ASR value also varies, even though the samples were all prepared the same way. Possible reasons for this could be better polishing for some samples or increased pressure when pressing the lithium on the single crystal, so it sticks to it and can be turned around to apply the second piece of lithium. It could also be a differing pressure in the Swagelok-like cell, where the impedance was measured, since the rubber insert tends to shrink after repeated heating and therefore the pressure decreases for subsequent samples.

Table 4.1: Change in ASR with temperature and time

Temperature [°C]	Heating time	ASR before [$\Omega \cdot cm^2$]	ASR after heating [$\Omega \cdot cm^2$]	Relative change [%]
175	1 h	6000	200	96.7
175	6 h	1000	20	98
120	1 h	650	150	77
175	6 h	2850	120	95.8
175	7 h	2370	30	98.7
175	7 h	1200	100	91.7
175	7 h	190	60	68.4
175	5 h	3400	250	92.6
175	7 h	1510	40	97.4
175	7 h	420	15	96.4

4.2 Available methods to determine the Critical Current density

There are three different measurements that could be used to determine the critical current density on symmetric lithium cells.

Method 1 - Current ramp

The first one is to apply a constantly rising current onto the sample. The current at which the potential drops due to dendrite growth, which culminates in a short circuit, denotes the CCD[25]. This method has the lowest measurement time, only limited by the sweep rate, but also the one where the result has to be interpreted with the most caution. The sign of the current does not change throughout the measurement, therefore only one side is stripped of lithium, which is then plated onto the other side. For that reason the results are mainly dependent on the interface quality of the side on which lithium is plated with voids leading to current constrictions and increased dendrite growth[45]. The continuous current change is the furthest removed from a realistic battery charging behaviour. Depending on the thickness of the sample and on the rate at which the current rises the resulting CCD may be higher than the real value, since the time for dendrite growth after initial filament formation is not taken into account. Furthermore there is no information about the capacity before a short circuit occurs. A model CCD measurement with this method is shown in Figure 4.8

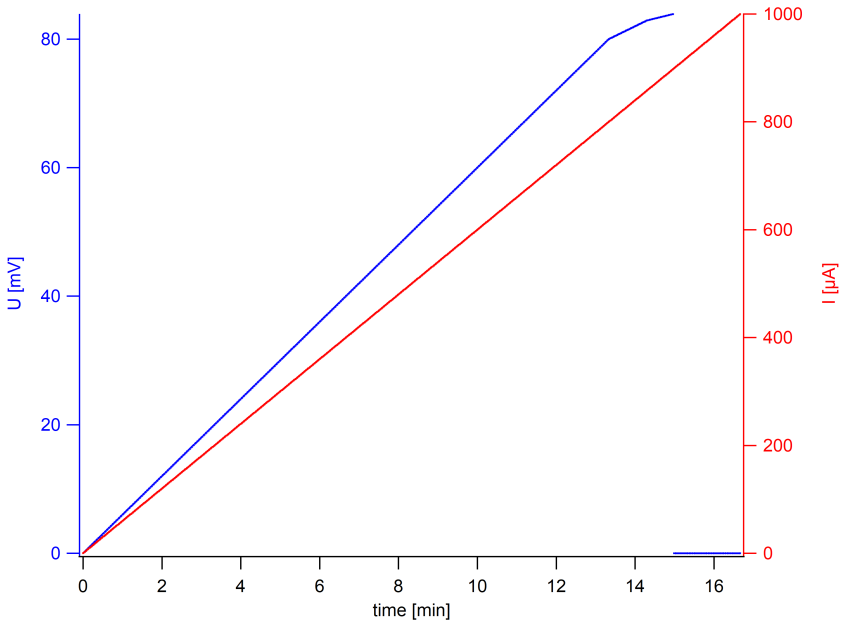

Figure 4.8: model CCD measurement with a current ramp.

Method 2 - Constant current steps, capacity disregarded

The second method is to cycle the cell with a constant current for a fixed, somewhat arbitrarily chosen, amount of time, increasing the current after each cycle. The measurement time is the highest, since the length of the measurement depends on the chosen time and the step size. The resolution with which the CCD can be determined, relies upon the step size. Depending on the chosen cycle duration, time is available for dendrite growth, so the tendency to overestimate the CCD is lower. The charging and discharging is closer to real battery behaviour but capacity is still disregarded. At higher currents the cycle time can therefore be longer than realistically used. A model CCD measurement with this method is shown in Figure 4.9

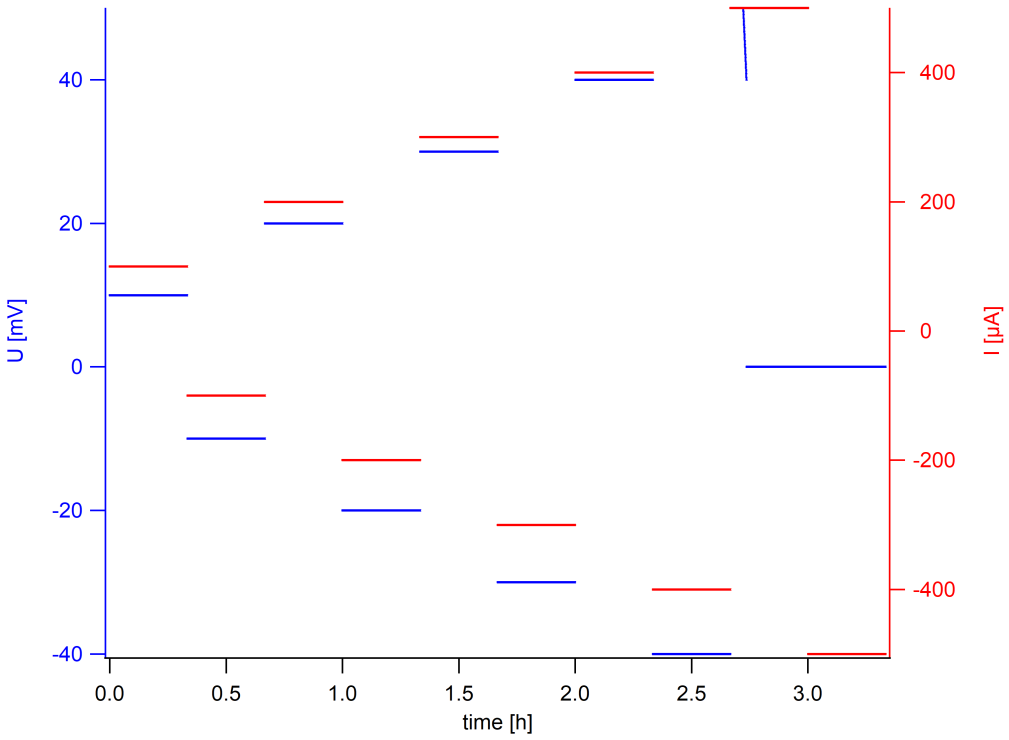

Figure 4.9: model CCD measurement with constant current increase, disregarding capacity.

Method 3 - Constant current steps, capacity taken into account

The last method is to cycle the cell with a constant current for a varying amount of time depending on a chosen capacity [46]. If the CCD of the sample is low, then this method is the slowest one, since at low currents a long time is needed to reach the capacity. At higher CCD values the total measurement time goes down, compared to the second method. The resolution is still dependent on the step size. There can also be a tendency

to overestimate the CCD, especially if the chosen capacity is rather small, resulting in low cycle times for higher currents. A model CCD measurement with this method is shown in Figure 4.10

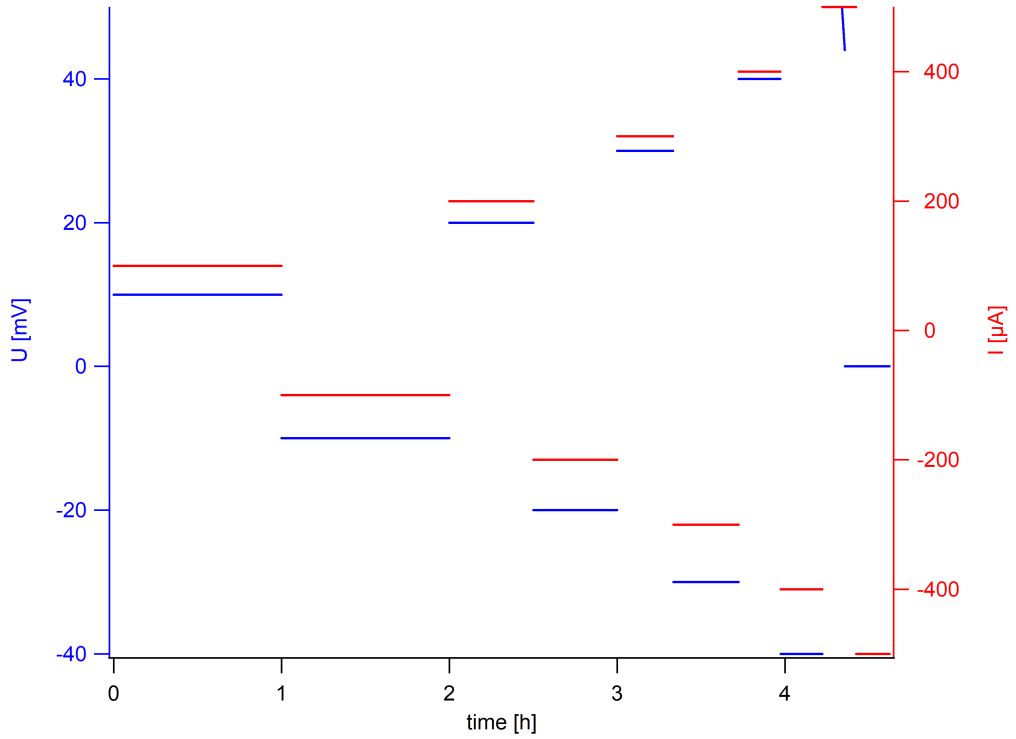

Figure 4.10: model CCD measurement with constant current increase, taking capacity into account.

Method 3 would be resembling realistic battery behaviour the most but long measurement times at low current densities are a significant drawback. No precise CCD value was known for LLZO single crystals, there is only a range of CCD values available for polycrystalline materials, shown in the next section. This necessitates a small step size to accurately determine the CCD, which led to the choice of method 2 for this work.

4.3 Critical Current Density Measurements - Different Interface Resistances

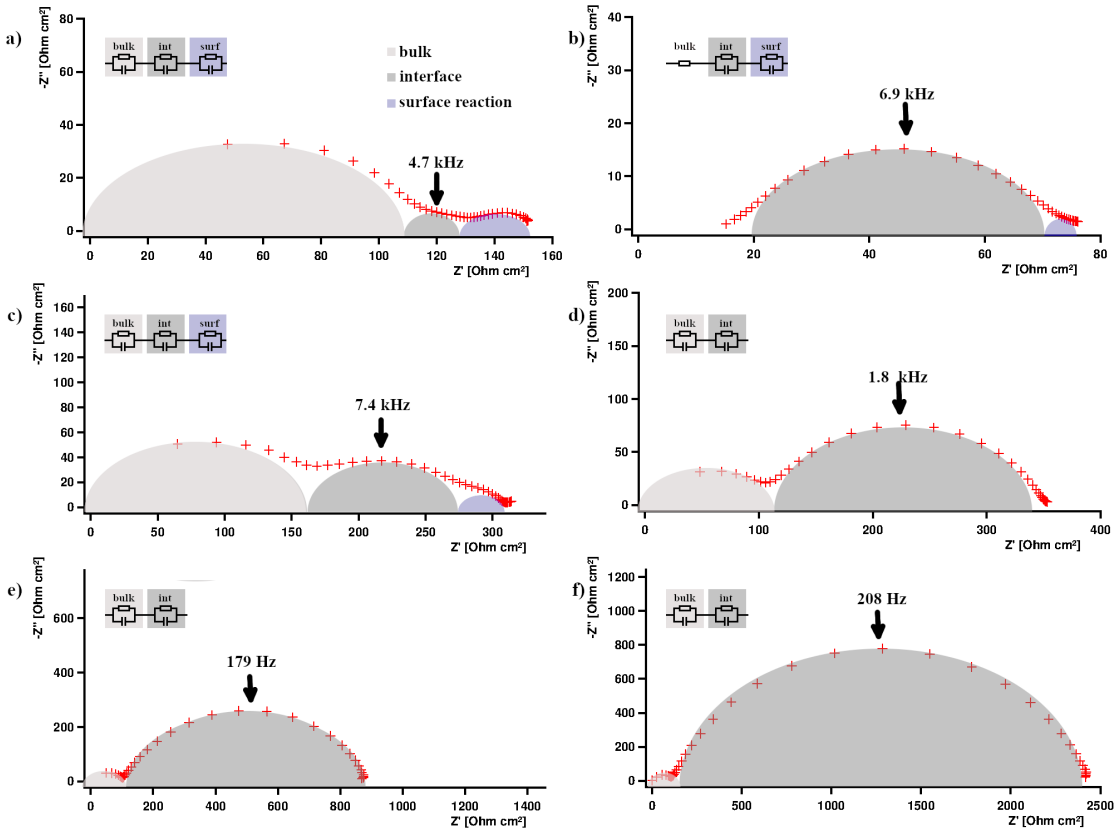

Figure 4.11: Nyquist plots of the six samples used. The equivalent circuits used to fit the data are depicted on the top left. The resonance frequency of the interface process is denoted. Semicircles have been added to approximately represent the individual contributions.

In the Figure 4.11 the Nyquist plots and the fits of the six samples, for which the critical current density was later determined, are shown. For the higher resistance samples there are only two semicircles visible. The high frequency one correspond to bulk processes, which can be seen in its capacitance, shown in table 4.2, which is in the pF range, whereas the capacitance for the low frequency semicircle is six orders of magnitude higher in the low µF range. For the low resistance samples a third semicircle appears, which might have been hidden in the interface semicircle at higher resistances. The third semicircle has a characteristic capacitance of 0.1 mF$\cdot cm^{-2}$. This corresponds to the capacitance of a chemical reaction[41], so it is likely a reaction of the lithium with the surface of the LLZO.

Table 4.2: Fitting parameters

Sample	Bulk capacitance pF$\cdot cm^{-2}$	ASR $\Omega \cdot cm^2$	Interface Capacitance nF$\cdot cm^{-2}$	CPE exponent
a)	279	13	1	0.8
b)	-	56	0.1	0.6
c)	300	116	0.09	0.6
d)	387	253	0.18	0.7
e)	445	797	0.56	0.7
f)	299	2335	0.16	0.7

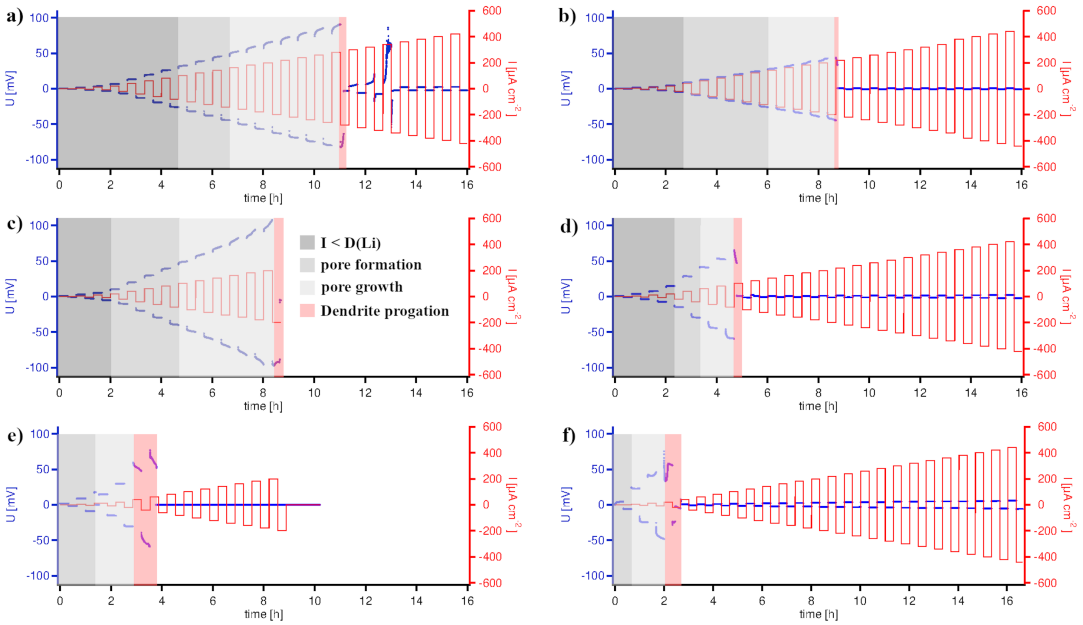

Figure 4.12: Current and voltage plotted against time for the six samples used.

Figure 4.12 shows the cycling plots of the six samples with the applied current and the measured potential plotted against the time. For sample e) there was a disconnect of the SMU after the second cycle, which is why the potential drops to zero, since no more current was applied. After this error was fixed, the cycling was resumed at the corresponding current density. The slightly lower potential after the restart could be due to relaxation processes in the cell during the downtime. There are four distinct regions visible, the width of each varying with the ASR of the sample. The first region is where there is ohmic behaviour and the potential is a parallel line to the current. Since there are no changes in the resistance it can be assumed that the contacted area at the interface remains the same and the lithium diffusion towards the interface is higher or equal to the lithium diffusion into the electrolyte. At the second region, there is a small increase in the resistance at the beginning of the cycle, which then plateaus. Here the lithium diffusion into the electrolyte is locally higher than the diffusion towards the interface and voids begin to form. Recent studies have found that the reason for this

is due to current constrictions at areas where the interface is not perfect[45]. Once the lithium in those areas has been removed, the contact area has been reduced and therefore the resistance increases but also the source of the current constriction is gone and this process stops during the cycle. During subsequent cycles lithium can again be plated over these voids, but not completely filling them, which might cause this behaviour to reoccur in subsequent cycles. In the third region, the current is high enough that the current constriction does not merely occur at isolated lithium parts at the interface, but also at the edges of the voids, enlarging them. This continuously increases the resistance due to reduced contact area and therefore the potential rises as well. Then there is the fourth region, where the resistance drops and a short circuit occurs. Here lithium dendrites propagate, decreasing the distance between the two electrodes, which in turn reduces the resistance. Once the lithium filament has bridged the gap between the electrodes, there are two possibilities. Either a hard short circuit occurs, where the potential drops to zero and remains at zero or it is a so called soft short circuit. Here the potential drops close to zero, but the cell can apparently still be cycled. This can be seen for the samples a), d) and f). A possible explanation could be, that the thin filament is molten due to Joule heating and the connection between the two electrodes is broken again[47]. The filament piece could then grow and melt again. Necessary for this would be that only one single piece of the dendrite bridges the gap, otherwise the current would be divided among the different pieces, leading to a reduced heating effect. To prove this, further experiments, like in operando temperature sensing of the sample, would be needed.

Table 4.3: ASR and impedance values of the samples used

Sample	ASR	CCD
a)	13 $\Omega \cdot cm^2$	280 $\mu A \cdot cm^2$
b)	56 $\Omega \cdot cm^2$	240 $\mu A \cdot cm^2$
c)	116 $\Omega \cdot cm^2$	200 $\mu A \cdot cm^2$
d)	253 $\Omega \cdot cm^2$	120 $\mu A \cdot cm^2$
e)	797 $\Omega \cdot cm^2$	60 $\mu A \cdot cm^2$
f)	2335 $\Omega \cdot cm^2$	40 $\mu A \cdot cm^2$

Table 4.3 shows the ASR values of the six samples and their determined CCD values. A clear improvement of the CCD can be seen with lower area specific resistance of the interface. In figure 4.13 the CCD is plotted against the ASR. A somewhat exponential behaviour for the CCD can be seen, which seems to reach its limit at around 300 $\mu A \cdot cm^2$. A recent publication predicted a theoretical limit according to a relaxation model, which suggests a stable current density region of up to 200 $\mu A \cdot cm^2$ at room temperature[45], which is in accordance with the obtained results.

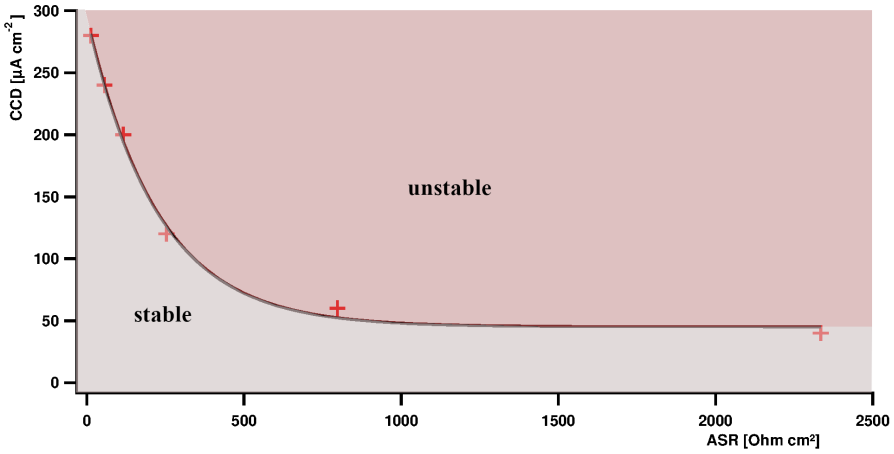

Figure 4.13: ASR plotted against the CCD of the six samples

4.4 Comparison with Literature

In Table 4.4 several CCD experiments for LLZO that have been found in literature are listed. The different annotations show noteworthy peculiarities. The ones noted with (1) use a Au interlayer. For (2) the grain size was the focus with SG for the small grained sample and LG for the large grained one. In (3) a porous structure was created with a surface area 40 times larger than the equivalent planar structure. Taking this into account leads to a CCD of 250 $\mu A \cdot cm^{-2}$. There are a few further problems regarding the comparability of these CCD values. First there is the composition of the samples. The dopants used to stabilize the cubic form of LLZO vary from Al[36][22][46][37][24], Ta[28][48], Ga[38] to Nb with Ca[49]. The listed compositions are also according to the given stoichiometric values in the respective papers. The produced and measured samples may differ in that regard. Since all of those are polycrystalline samples density and grain size is also not uniform, the latter not even mentioned in most cases[36][37]. The area specific resistance and the sample preparation needed to achieve those values, differs in each paper. Then there is the method used to determine the critical current density, which varies in measurement setup, measurement program, temperature and applied pressure.

Table 4.4: Critical current density values and experimental conditions reported in literature.

Composition	ρ_{rel} $[g \cdot cm^{-3}]$	ASR $[\Omega \cdot cm^2]$	CCD $[\mu A \cdot cm^{-2}]$	T [°C]	p [MPa]	Ref.
$Li_{6.25}Al_{0.25}La_3Zr_2O_{12}$ (1)	>99	9-15	900±700	25	3.3	[36]
$Li_{6.5}Al_{0.15}La_3Zr_{1.5}Ta_{0.5}O_{12}$ (1)	>99	9-15	900±700	25	3.3	[36]
$Li_{6.25}Al_{0.25}La_3Zr_2O_{12}$	97±1	514	50	30	0.35	[22]
$Li_{6.25}Al_{0.25}La_3Zr_2O_{12}$	-	10	930±240	25	3.4	[46]
$Li_{6.25}Al_{0.25}La_3Zr_2O_{12}$	96.0-99.4	2-5	300-600	RT	3.5	[50]
$Li_{6.25}Al_{0.25}La_3Zr_2O_{12}$ LG (2)	90	130	46	RT	0.2	[37]
$Li_{6.25}Al_{0.25}La_3Zr_2O_{12}$ SG (2)	92	37	134	RT	0.2	[37]
$Li_{6.5}La_3Zr_{1.5}Ta_{0.5}O_{12}$	96	69-363	200-400	25	1.4	[28]
$Li_{6.5}La_3Zr_{1.5}Ta_{0.5}O_{12}$	95.8-96.6	47-69	150-600	25	1.4	[48]
$Li_{6.55}Ga_{0.15}La_3Zr_2O_{12}$	95	16.7	160	RT	coin cell	[38]
$Li_{6.55}Al_{0.15}La_3Zr_2O_{12}$	95	12.1	100	RT	coin cell	[38]
$Li_{6.6}Al_{0.15}La_3Zr_{1.6}Ta_{0,4}O_{12}$ (1)	99	380	500	25	0.1	[27]
$Li_{6.25}Al_{0.25}La_3Zr_2O_{12}$	97±1	200	100	25	0.32	[24]
$Li_{6.75}La_{2.75}Ca_{0.25}Zr_{1.5}Nb_{0.5}O_{12}$ (3)	99	7	10000	RT	button cell	[49]

5 Summary and outlook

To conclude, the reduction of the ASR in the Li-LLZO-Li system was tested and accomplished with different methods found in literature. The usage of a gold interlayer reduced the ASR but a deliberate variation was not possible. Heating the samples after assembly also lowered the ASR and it was possible to vary the ASR but no precise correlation between the heating time, the temperature and the relative ASR change was found.
Cycling experiments were done of six samples with varying ASR values until a short circuit occurred, which denotes the critical current density. A correlation between the ASR and the CCD was determined. An upper CCD limit for a LLZO sample without the application of significant pressure and other external factors was found at 300 $\mu A \cdot cm^2$, which is in accord with theoretically predicted limit, obtained using a relaxation model of 200 $\mu A \cdot cm^2$ from literature[45]. The comparison with other CCD values reported in literature is difficult if not impossible, due to differences in composition, density, the usage of single crystals instead of polycrystalline samples and differences in the method to determine the CCD. In order to further improve the critical current density, either an increase in the working temperature, the application of significant pressure onto the sample or additional surface modification would be needed. The use of a porous structure to increase the surface area as reported by Hitz[49] would be one possible modification. A possible continuation of this work could be to vary the pressure on the Li|LLZO|Li sample and measure the ASR and the CCD as a function of stack pressure.

Bibliography

[1] Catia Arbizzani, Giulio Gabrielli, and Marina Mastragostino. Thermal stability and flammability of electrolytes for lithium-ion batteries. *Journal of Power Sources*, 196(10):4801–4805, 2011.

[2] Amer Hammami, Nathalie Raymond, and Michel Armand. Runaway risk of forming toxic compounds. *Nature*, 424(6949):635–636, 2003.

[3] John B Goodenough and Youngsik Kim. Challenges for rechargeable batteries. *Journal of Power Sources*, 196(16):6688–6694, 2011.

[4] Ryoji Kanno and Masahiro Murayama. Lithium ionic conductor thio-lisicon: the li2 s ges2 p 2 s 5 system. *Journal of the electrochemical society*, 148(7):A742–A746, 2001.

[5] Noriaki Kamaya, Kenji Homma, Yuichiro Yamakawa, Masaaki Hirayama, Ryoji Kanno, Masao Yonemura, Takashi Kamiyama, Yuki Kato, Shigenori Hama, Koji Kawamoto, et al. A lithium superionic conductor. *Nature materials*, 10(9):682–686, 2011.

[6] Yutao Li, Jian-Tao Han, Chang-An Wang, Hui Xie, and John B Goodenough. Optimizing li+ conductivity in a garnet framework. *Journal of Materials Chemistry*, 22(30):15357–15361, 2012.

[7] Junji Awaka, Norihito Kijima, Hiroshi Hayakawa, and Junji Akimoto. Synthesis and structure analysis of tetragonal li7la3zr2o12 with the garnet-related type structure. *Journal of solid state chemistry*, 182(8):2046–2052, 2009.

[8] Venkataraman Thangadurai, Dana Pinzaru, Sumaletha Narayanan, and Ashok Kumar Baral. Fast solid-state li ion conducting garnet-type structure metal oxides for energy storage. *The journal of physical chemistry letters*, 6(2):292–299, 2015.

[9] Jan L Allen, Jeffrey Wolfenstine, Ezhiylmurugan Rangasamy, and Jeff Sakamoto. Effect of substitution (ta, al, ga) on the conductivity of li7la3zr2o12. *Journal of Power Sources*, 206:315–319, 2012.

[10] Travis Thompson, Seungho Yu, Logan Williams, Robert D Schmidt, Regina Garcia-Mendez, Jeff Wolfenstine, Jan L Allen, Emmanouil Kioupakis, Donald J Siegel, and Jeff Sakamoto. Electrochemical window of the li-ion solid electrolyte li7la3zr2o12. *ACS Energy Letters*, 2(2):462–468, 2017.

[11] Fudong Han, Yizhou Zhu, Xingfeng He, Yifei Mo, and Chunsheng Wang. Electrochemical stability of li10gep2s12 and li7la3zr2o12 solid electrolytes. *Advanced Energy Materials*, 6(8):1501590, 2016.

[12] Daniel Rettenwander, Guenther Redhammer, Florian Preishuber-Pfluegl, Lei Cheng, Lincoln Miara, Reinhard Wagner, Andreas Welzl, Emmanuelle Suard, Marca M Doeff, Martin Wilkening, et al. Structural and electrochemical consequences of al and ga cosubstitution in li7la3zr2o12 solid electrolytes. *Chemistry of materials*, 28(7):2384–2392, 2016.

[13] Asma Sharafi, Eric Kazyak, Andrew L Davis, Seungho Yu, Travis Thompson, Donald J Siegel, Neil P Dasgupta, and Jeff Sakamoto. Surface chemistry mechanism of ultra-low interfacial resistance in the solid-state electrolyte li7la3zr2o12. *Chemistry of Materials*, 29(18):7961–7968, 2017.

[14] Ramaswamy Murugan, Venkataraman Thangadurai, and Werner Weppner. Fast lithium ion conduction in garnet-type li7la3zr2o12. *Angewandte Chemie International Edition*, 46(41):7778–7781, 2007.

[15] K Brandt. Historical development of secondary lithium batteries. *Solid State Ionics*, 69(3-4):173–183, 1994.

[16] Martin Winter, Jürgen O Besenhard, Michael E Spahr, and Petr Novak. Insertion electrode materials for rechargeable lithium batteries. *Advanced materials*, 10(10):725–763, 1998.

[17] Martin Winter and Jürgen O Besenhard. Wiederaufladbare batterien. *Chemie in unserer Zeit*, 33(5):252–266, 1999.

[18] Philippe Knauth. Inorganic solid li ion conductors: An overview. *Solid State Ionics*, 180(14-16):911–916, 2009.

[19] William D Richards, Lincoln J Miara, Yan Wang, Jae Chul Kim, and Gerbrand Ceder. Interface stability in solid-state batteries. *Chemistry of Materials*, 28(1):266–273, 2016.

[20] Charles Monroe and John Newman. The impact of elastic deformation on deposition kinetics at lithium/polymer interfaces. *Journal of The Electrochemical Society*, 152(2):A396–A404, 2005.

[21] Yaoyu Ren, Yang Shen, Yuanhua Lin, and Ce-Wen Nan. Direct observation of lithium dendrites inside garnet-type lithium-ion solid electrolyte. *Electrochemistry Communications*, 57:27–30, 2015.

[22] Asma Sharafi, Harry M Meyer, Jagjit Nanda, Jeff Wolfenstine, and Jeff Sakamoto. Characterizing the li–li7la3zr2o12 interface stability and kinetics as a function of temperature and current density. *Journal of Power Sources*, 302:135–139, 2016.

[23] K Ishiguro, Y Nakata, M Matsui, I Uechi, Y Takeda, O Yamamoto, and N Imanishi. Stability of nb-doped cubic li7la3zr2o12 with lithium metal. *Journal of The Electrochemical Society*, 160(10):A1690–A1693, 2013.

[24] Eric Jianfeng Cheng, Asma Sharafi, and Jeff Sakamoto. Intergranular li metal propagation through polycrystalline li6. 25al0. 25la3zr2o12 ceramic electrolyte. *Electrochimica Acta*, 223:85–91, 2017.

[25] Lukas Porz, Tushar Swamy, Brian W Sheldon, Daniel Rettenwander, Till Frömling, Henry L Thaman, Stefan Berendts, Reinhard Uecker, W Craig Carter, and Yet-Ming Chiang. Mechanism of lithium metal penetration through inorganic solid electrolytes. *Advanced Energy Materials*, 7(20):1701003, 2017.

[26] Guanchen Li and Charles W Monroe. Dendrite nucleation in lithium-conductive ceramics. *Physical Chemistry Chemical Physics*, 21(36):20354–20359, 2019.

[27] Chih-Long Tsai, Vladimir Roddatis, C Vinod Chandran, Qianli Ma, Sven Uhlenbruck, Martin Bram, Paul Heitjans, and Olivier Guillon. Li7la3zr2o12 interface modification for li dendrite prevention. *ACS applied materials & interfaces*, 8(16):10617–10626, 2016.

[28] Rajendra Hongahally Basappa, Tomoko Ito, and Hirotoshi Yamada. Contact between garnet-type solid electrolyte and lithium metal anode: influence on charge transfer resistance and short circuit prevention. *Journal of The Electrochemical Society*, 164(4):A666–A671, 2017.

[29] Alan C Luntz, Johannes Voss, and Karsten Reuter. Interfacial challenges in solid-state li ion batteries, 2015.

[30] Xiaogang Han, Yunhui Gong, Kun Kelvin Fu, Xingfeng He, Gregory T Hitz, Jiaqi Dai, Alex Pearse, Boyang Liu, Howard Wang, Gary Rubloff, et al. Negating interfacial impedance in garnet-based solid-state li metal batteries. *Nature materials*, 16(5):572–579, 2017.

[31] Yutao Li, Weidong Zhou, Xi Chen, Xujie Lü, Zhiming Cui, Sen Xin, Leigang Xue, Quanxi Jia, and John B Goodenough. Mastering the interface for advanced all-solid-state lithium rechargeable batteries. *Proceedings of the National Academy of Sciences*, 113(47):13313–13317, 2016.

[32] Bingbin Wu, Shanyu Wang, Willie J Evans IV, Daniel Z Deng, Jihui Yang, and Jie Xiao. Interfacial behaviours between lithium ion conductors and electrode materials in various battery systems. *Journal of Materials Chemistry A*, 4(40):15266–15280, 2016.

[33] Kazunori Takada, Narumi Ohta, Lianqi Zhang, Xiaoxiong Xu, Bui Thi Hang, Tsuyoshi Ohnishi, Minoru Osada, and Takayoshi Sasaki. Interfacial phenomena in solid-state lithium battery with sulfide solid electrolyte. *Solid State Ionics*, 225:594–597, 2012.

[34] Jun Haruyama, Keitaro Sodeyama, Liyuan Han, Kazunori Takada, and Yoshitaka Tateyama. Space–charge layer effect at interface between oxide cathode and sulfide electrolyte in all-solid-state lithium-ion battery. *Chemistry of Materials*, 26(14):4248–4255, 2014.

[35] Arpa-e | ionics. Accessed: 15.05.2020.

[36] Nathan J Taylor, Sandra Stangeland-Molo, Catherine G Haslam, Asma Sharafi, Travis Thompson, Michael Wang, Regina Garcia-Mendez, and Jeff Sakamoto. Demonstration of high current densities and extended cycling in the garnet li7la3zr2o12 solid electrolyte. *Journal of Power Sources*, 396:314–318, 2018.

[37] Lei Cheng, Wei Chen, Martin Kunz, Kristin Persson, Nobumichi Tamura, Guoying Chen, and Marca Doeff. Effect of surface microstructure on electrochemical performance of garnet solid electrolytes. *ACS applied materials & interfaces*, 7(3):2073–2081, 2015.

[38] Federico M Pesci, Rowena H Brugge, AK Ola Hekselman, Andrea Cavallaro, Richard J Chater, and Ainara Aguadero. Elucidating the role of dopants in the critical current density for dendrite formation in garnet electrolytes. *Journal of Materials Chemistry A*, 6(40):19817–19827, 2018.

[39] L Yuan, HK Liu, A Maaroof, K Konstantinov, J Liu, and M Cortie. Mesoporous gold as anode material for lithium-ion cells. *Journal of New Materials for Electrochemical Systems*, 2007.

[40] M Zafar A Munshi. *Handbook of solid state batteries and capacitors*. World Scientific, 1995.

[41] D.C. Irvine, J.T.S Sinclair and A.R. West. Electroceramics: Characterization by impedance spectroscopy. *Adv. Mater*, 2:132–138, 1990.

[42] Jung-Ki Park. *Principles and applications of lithium secondary batteries*. John Wiley & Sons, 2012.

[43] Kun Kelvin Fu, Yunhui Gong, Boyang Liu, Yizhou Zhu, Shaomao Xu, Yonggang Yao, Wei Luo, Chengwei Wang, Steven D Lacey, Jiaqi Dai, et al. Toward garnet electrolyte–based li metal batteries: An ultrathin, highly effective, artificial solid-state electrolyte/metallic li interface. *Science Advances*, 3(4):e1601659, 2017.

[44] Chengwei Wang, Yunhui Gong, Boyang Liu, Kun Fu, Yonggang Yao, Emily Hitz, Yiju Li, Jiaqi Dai, Shaomao Xu, Wei Luo, et al. Conformal, nanoscale zno surface modification of garnet-based solid-state electrolyte for lithium metal anodes. *Nano letters*, 17(1):565–571, 2017.

[45] Thorben Krauskopf, Hannah Hartmann, Wolfgang G Zeier, and Juergen Janek. Toward a fundamental understanding of the lithium metal anode in solid-state batteries—an electrochemo-mechanical study on the garnet-type solid electrolyte li6. 25al0. 25la3zr2o12. *ACS applied materials & interfaces*, 11(15):14463–14477, 2019.

[46] Michael Wang, Jeffrey B Wolfenstine, and Jeff Sakamoto. Temperature dependent flux balance of the li/li7la3zr2o12 interface. *Electrochimica Acta*, 296:842–847, 2019.

[47] William Manalastas Jr, Jokin Rikarte, Richard J Chater, Rowena Brugge, Ainara Aguadero, Lucienne Buannic, Anna Llordés, Frederic Aguesse, and John Kilner. Mechanical failure of garnet electrolytes during li electrodeposition observed by in-operando microscopy. *Journal of Power Sources*, 412:287–293, 2019.

[48] Rajendra Hongahally Basappa, Tomoko Ito, Takao Morimura, Raman Bekarevich, Kazutaka Mitsuishi, and Hirotoshi Yamada. Grain boundary modification to suppress lithium penetration through garnet-type solid electrolyte. *Journal of Power Sources*, 363:145–152, 2017.

[49] Gregory T Hitz, Dennis W McOwen, Lei Zhang, Zhaohui Ma, Zhezhen Fu, Yang Wen, Yunhui Gong, Jiaqi Dai, Tanner R Hamann, Liangbing Hu, et al. High-rate lithium cycling in a scalable trilayer li-garnet-electrolyte architecture. *Materials Today*, 22:50–57, 2019.

[50] Asma Sharafi, Catherine G Haslam, Robert D Kerns, Jeff Wolfenstine, and Jeff Sakamoto. Controlling and correlating the effect of grain size with the mechanical and electrochemical properties of li 7 la 3 zr 2 o 12 solid-state electrolyte. *Journal of Materials Chemistry A*, 5(40):21491–21504, 2017.